http://dx.doi.org/10.5935/0103-5053.20150344

*J. Braz. Chem. Soc.*, Vol. 27, No. 2, 423-433 2016.
Printed in Brazil - ©2016 Sociedade Brasileira de Química
0103 - 5053 $6.00+0.00

Article

# Ultrafast Dynamics of Au Nanopyramid Interfaces Prepared by Nanosphere Lithography: Effect of Substrate Chemical Composition

***Guilherme F. Ferbonink,[a] Edna R. Spada,[b] Diego P. dos Santos,[a] Maria L. Sartorelli[c] and Rene A. Nome*[,a]***

[a]*Instituto de Química, Universidade Estadual de Campinas, CP 6154, 13083-970 Campinas-SP, Brazil*

[b]*Departamento de Física, Centro de Ciências Físicas e Matemáticas, Universidade Federal de Santa Catarina, 88040-900 Florianópolis-SC, Brazil*

[c]*Instituto de Física de São Carlos, Universidade de São Paulo, 13566-590 São Carlos-SP, Brazil*

This work describes ultrafast spectroscopy studies of Au triangular pyramid particle arrays deposited over glass (termed Au/glass), and 190 nm indium tin oxide (ITO) film (termed Au/ITO/glass) prepared by nanosphere lithography. The linear absorption spectra of Au/glass and Au/ITO/glass exhibit surface plasmon resonances at 800 and 870 nm, respectively, in good agreement with discrete dipole approximation simulations. Ultrafast pump-probe measurements at wavelengths below resonance, at resonance, and above the surface plasmon resonance for each of these two systems are presented. The pump-probe measurements on both systems can be well fit with a model accounting for electron-electron scattering, electron-phonon coupling, and acoustic oscillations on top of cooling of the gold lattice. Numerical simulations employing a two-temperature model are consistent with the single-color pump-probe exponential decays. The wavelength-dependent pump-probe results are interpreted in terms of the complex wavelength-dependent refractive index of gold. We show that this interpretation is consistent with diffractive-optic four-wave mixing spectroscopy measurements of absorptive and dispersive parts of the third-order nonlinear polarization at 800 nm.

**Keywords:** ultrafast spectroscopy, interface processes, nanomaterials

## Introduction

At the surface plasmon resonance of a metal nanoparticle, excited conduction electrons are confined to the interface between metal and dielectric.[1] As a result, metallic nanoparticles can efficiently concentrate optical radiation into a small volume leading to high local field enhancement factors. The optical properties of gold nanoparticles have been employed in wide-ranging applications, including sensing,[2] biomedicine,[3,4] catalysis,[5] and nanophotonics.[6] The variety of applications of surface plasmon resonances stem in part from the ability to control the electronic and optical properties of metallic nanoparticles, employing either top-down or bottom-up approaches to tailor sizes, geometries, and shapes of metallic nanoparticles and particle arrays.[7]

The application of plasmonics to high-performance photovoltaic devices is a promising area of research.[8] In a recent example of nanoscale plasmonic solar-cell engineering, poly(3-hexylthiophene) (P3HT), an organic photovoltaic absorber, was integrated in the gap between the arms of a plasmonic antenna array, thus forming an array from an axial heterostructure of metal and P3HT.[9] Light is concentrated in the nanoscale gap between the two antenna arms, and photocurrent is generated in the P3HT semiconductor. Despite extensive recent research on this topic, significant improvement of solar cells due to replacement of dielectrics with plasmonic materials is yet to be demonstrated and understood.

In order to minimize the large losses inherently associated with metals, plasmonic solar cells have also been investigated using alternative plasmonic materials, such as metal alloys and heavily doped semiconductors.[10] For example, recent work has investigated picosecond optical excitation of indium tin oxide (ITO)-Au plasmonic nanoantennas as a means for locally modulating the free-carrier density.[11] The authors have identified an ultrafast response of the

*e-mail: nome@iqm.unicamp.br

antenna-ITO hybrid system, which is distinctly different from transient bleaching observed for gold antennas on a non-conducting $SiO_2$ substrate.[11] The results were explained by the large free-carrier nonlinearity of ITO, which is enhanced by plasmon-induced hot-electron injection from the gold nanoantenna into the conductive oxide. Ultrafast interfacial charge injection has also been described in related systems, including plasmon-induced ultrafast charge injection in gold nanoparticle/$TiO_2$,[12] and charge-transfer in a chromophore sensitized $TiO_2$ nanocomposite.[13]

In the present work, we report ultrafast measurements of Au-ITO hybrids, in which Au triangular pyramid particle-arrays are deposited over ITO films by nanosphere lithography. The same fabrication procedure and time-resolved experiments were used to investigate the ultrafast dynamics of Au arrays deposited over glass, so that a direct comparison between the two systems can be made. The linear absorption spectra of Au/glass and Au/ITO/glass exhibit maximum absorption peaks at 800 and 870 nm, respectively, which are attributed to dipolar surface plasmon resonance peaks. For each of these two systems, we have measured the ultrafast pump-probe dynamics at the surface plasmon resonance, and above and below the surface plasmon resonance frequency. Four-wave mixing spectroscopy measurements at 800 nm are consistent with the pump-probe data. Our results are supported by numerical simulations of the linear optical response and of the thermal evolution of electron and lattice temperatures.

## Results and Discussion

The great advantage of using the spin coating technique in the preparation of colloidal masks is speed: preparation time of a mask is approximately 3 min and allows parameter control to obtain masks formed strictly by a monolayer of polystyrene spheres. However, scanning electron microscopy (SEM) images of the mask (Figure 1a) show defects in sphere packing. Once the Au layer was evaporated and the polystyrene mask removed, the "memory" of such defects remains in the triangular prism array of Au nanoparticles. Figure 1b shows SEM images of Au islands after removal of the polystyrene mask. The area shown in Figure 1b is 1 $mm^2$ while the total area of the nanostructure array is approximately 1 $cm^2$; the homogeneity throughout the entire sample is similar to that shown in Figure 1b.

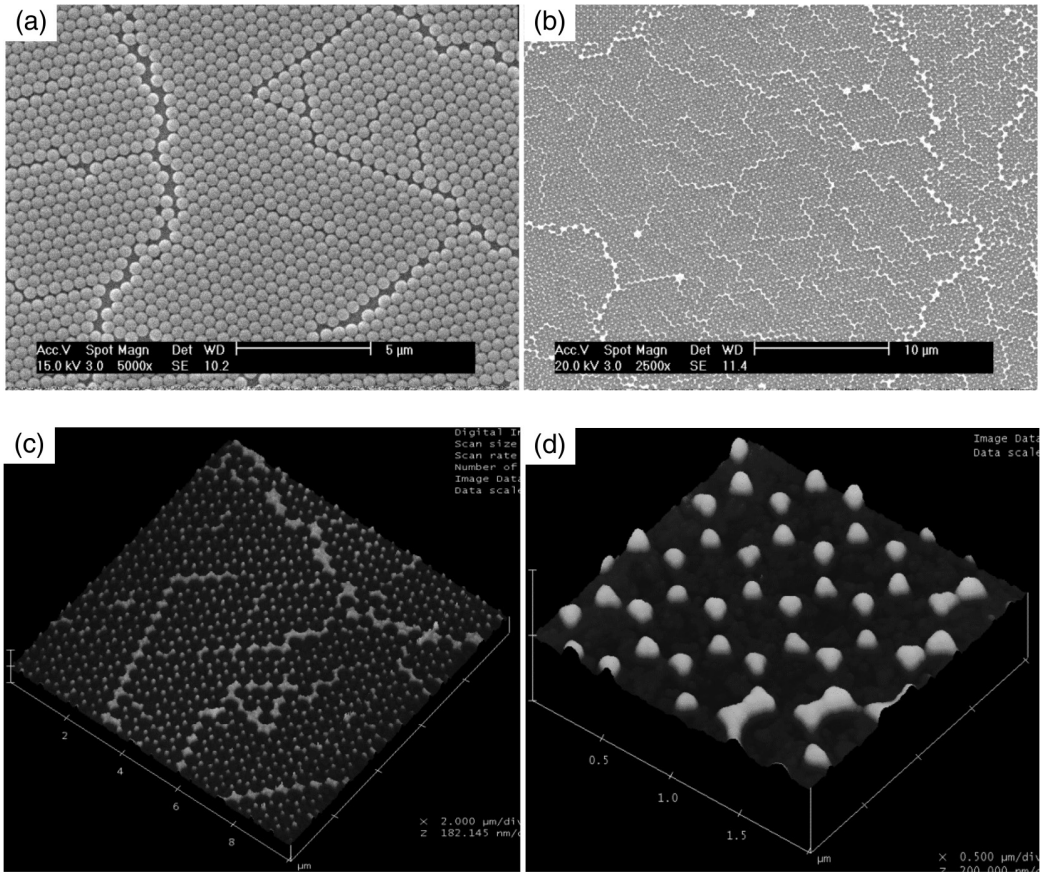


**Figure 1.** SEM images of (a) the mask and (b) islands of Au after removal of the polystyrene (PS) mask. (c) and (d) 3D AFM images of the Au islands in scale of 10 and 2 µm, respectively.

Atomic force microscopy (AFM) images show the overall good uniformity of the Au nanoparticle triangular prism array, although other morphologies such as bowtie-like particle dimers can also be seen, as shown in Figures 1c and 1d. Regarding the ultrafast spectroscopy measurements, lateral movement of sample position led to small changes in the retrieved kinetic parameters, presumably due to signals from defects such as bowtie. Although we have not quantified the amount of defects, we believe contribution of defects to the observed signals is small, since large heterogeneity in particle shape would lead to dephasing in the acoustic oscillations of individual nanoparticles.[14] Thus, coherent oscillations observed in the pump-probe and four-wave mixing measurements suggest that the samples consist mostly of homogeneously distributed and isolated Au particles.

As indicated in Figure 2, quantitative analysis of the images obtained by AFM shows that the average height of the islands obtained was 45 ± 5 nm. This particle height is in good agreement with the thickness of evaporated Au, which was 50 nm, as monitored using a quartz microbalance coupled to the evaporation chamber. Approximating the islands as triangles, the triangle base ($l\sqrt{3}/2$) is about 220 ± 15 nm as shown in Figure 2b. Also, quantitative analysis of the AFM image shown in Figure 2a indicates an average gap (distance between tips of neighboring nanoparticle islands) greater than 50 nm. A previous experimental and computational work on Au bipyramidal nanoparticle dimers with dimensions similar to those reported in the present work indicated negligible plasmonic interactions and optical forces for gaps greater than 15 nm, even for head-to-tail nanoparticle dimer geometries.[15] Moreover, interparticle coupling effects on the ultrafast dynamics of Au monolayer periodic nanoprism arrays have also been discussed,[16] and the ultrafast spectroscopy results presented below show that our sample consists mostly of isolated (non-interacting) Au islands.

Figure 3a shows linear absorption spectra of Au islands on glass (Au/glass, black dashed curve), Au islands on ITO/glass (Au/ITO/glass, red curve), as well as absorption spectra of the substrates (glass and ITO/glass). The Au/glass spectrum displays a strong absorption band centered at 800 nm, a weaker transition around 590 nm, and a broad, weak absorption near 410 nm. The absorption spectrum of Au/ITO/glass displays qualitatively similar features: an absorption maximum at 870 nm, a broad structure-less band near 640 nm, and a weaker band near 430 nm. Thus, the Au/glass and Au/ITO/glass spectra display similar-looking features. The main differences between the two spectra are: (*i*) a redshift and peak broadening of the near-infrared (IR) absorption band in going from Au/glass to Au/ITO/glass; (*ii*) a small redshift in the absorption band for Au/ITO/glass near 640 nm; and (*iii*) a more clearly defined band near 430 nm for Au/ITO/glass. The results shown in Figure 3a

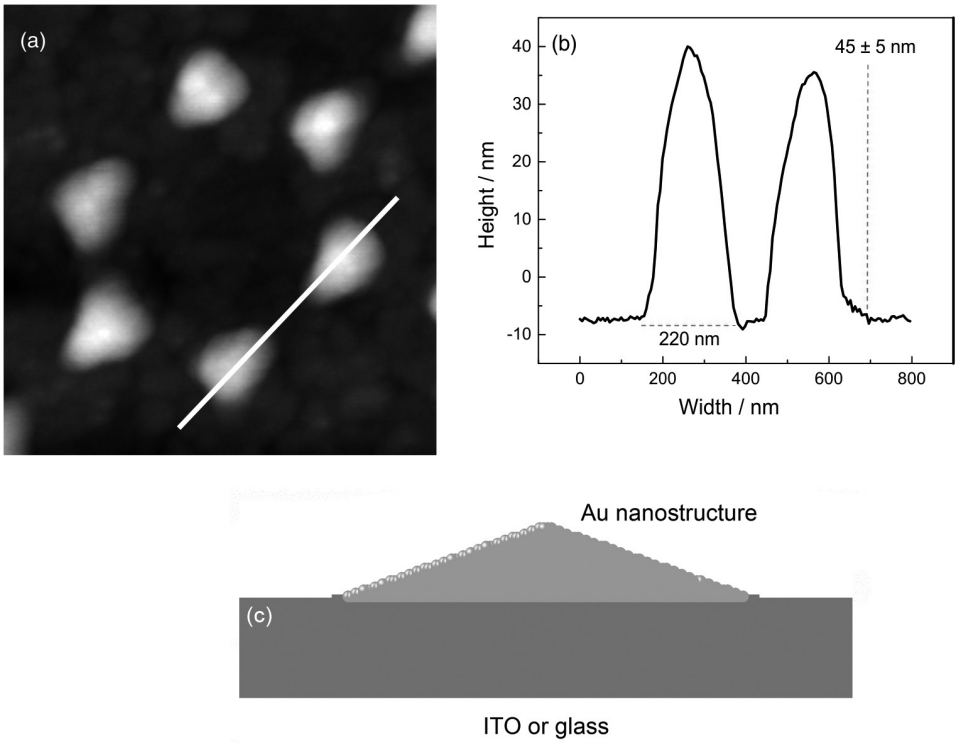


**Figure 2.** (a) Tapping mode AFM image and (b) line scan of Au islands arrays on ITO substrate (without corrections for the effects of tip); (c) Model of Au islands (orange triangle) deposited over ITO or glass (gray rectangle) used as simulation target shape in discrete dipole approximation (DDA) simulations.

are consistent with discrete dipole approximation (DDA) simulations shown in Figure 3b.

In general, the position and width of the plasmon resonance peak depends on the material, shape and size of the nanoparticles, which allows adjustment of the peak in the spectral region from visible to the near-IR.[17-19] All of these spectroscopic features may be explained by substrate dielectric constant effects on the optical properties of metal nanoparticles. That is, differences in refractive index of ITO *vs.* glass leads to a redshift in the absorption spectra.[20] Both glass and ITO/glass display negligible absorption in the near-800 nm wavelength range of interest, as shown in Figure 3a.

The absorption maximum at 800 nm is assigned to dipolar plasmon resonance of the Au nanoparticles, consistent with previously reported data for similar nanostructures prepared by nanosphere lithography.[21] Given the geometry of the Au islands, the 800 nm band is attributed to longitudinal plasmon mode excitation along the nano-pyramid base, which is in contact with the glass substrate. At higher energies, the weaker 600 nm band is attributed to quadrupolar plasmon excitation whereas the inter-band transition is observed near 410 nm.[21] Similarly, for the Au/ITO/glass sample, we observe dipolar longitudinal plasmon excitation, quadrupolar resonance, and interband transitions near 870, 640, and 430 nm, respectively. The surface plasmon resonance wavelength redshifts as the refractive index of the surrounding environment is increased.[20] Neglecting the wavelength-dependence of the refractive index, the substrate refractive index in the near-IR is *n* ca. 1.55 for glass and *n* ca. 1.75 for ITO. The measured redshift in going from Au/glass to Au/ITO/glass is approximately 70 nm (from 800 to 870 nm). We also note that the higher dielectric constant of ITO *vs.* glass also leads to an increase in the surface plasmon resonance linewidth due to radiation damping.[22,23] These considerations are generally consistent with the numerical results from DDA simulations, even though the wavelength-dependent refractive index of ITO cannot be neglected.

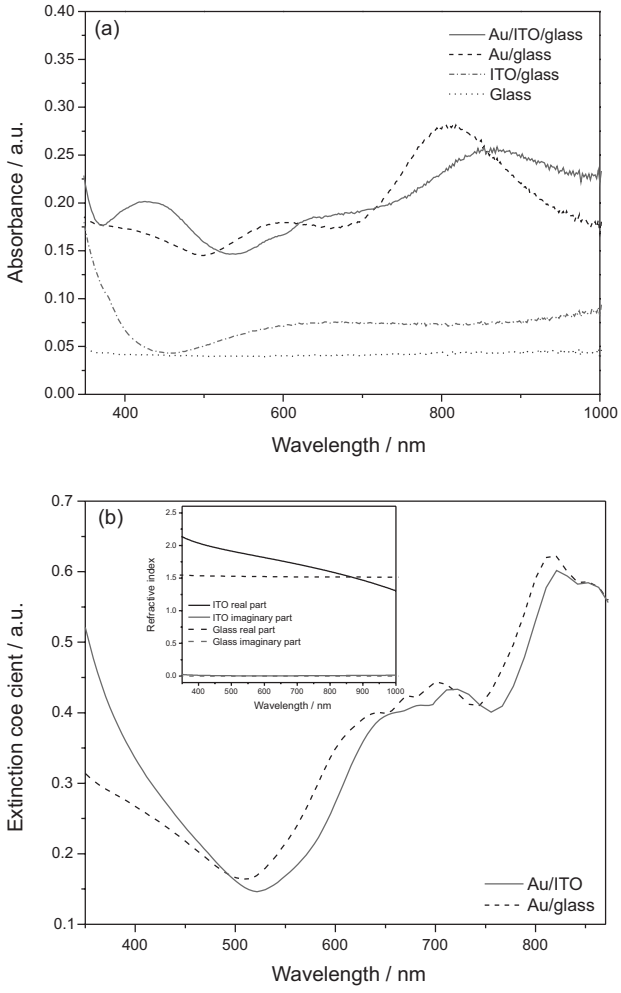


**Figure 3.** (a) UV-Vis absorption spectra of Au/glass (black), Au/ITO/glass (red), ITO/glass (gray), and glass (blue). (b) DDA simulated extinction spectra for Au/glass (black) and Au_ITO (red). Inset: real (black) and imaginary (red) refractive index for ITO (full line) and glass (dashed line).

Figure 3b shows the simulated extinction spectra for a single Au island over ITO (Au/ITO, red curve) and over glass (Au/glass, black curve). The simulations results show a very good qualitative agreement with the experimental spectra in Figure 3a. A signal due to Au interband absorption and scattering by the substrate, specially ITO, is observed around 400 nm, whose refractive index is larger in that region, as can be observed in the inset of Figure 3b. Additionally, resonances around 650 and 800 nm were observed in the simulations as in the experimental results, which were attributed to quadrupolar and dipolar plasmon modes, respectively. Such plasmon resonances were redshifted for the Au/ITO system in comparison with Au/glass, in qualitative agreement with experimental results. Such redshift can be attributed to the differences in the refractive index for the substrates supporting the Au islands. As can be seen in the inset of Figure 3b, the real part of the ITO refractive index is larger than that of glass up to 800 nm. Although the simulations results show a redshift for the plasmon resonances, the shift observed for the dipolar mode was larger in the experimental results than in the simulations, which can be attributed to possible differences in the real and simulated Au island shapes, as well as possible heterogeneities among Au/ITO and Au/glass samples.

Figure 4a displays the 800 nm pump/800 nm probe signals for Au/glass and Au/ITO/glass for the first 100 ps following excitation. The results shown in Figure 4a were performed with 50 fs pulse duration laser pulses, as measured by frequency-resolved optical gating (Figure 4a,

inset). Table 1 summarizes the amplitude, time constants, and oscillation periods obtained by least-squares nonlinear fitting of the pump-probe data shown in Figures 4a and 5b for Au/glass and Au/ITO/glass. The Au/glass sample (black curve in Figure 4a) exhibits (*i*) a femtosecond decay constant following pump excitation; (*ii*) relaxation times of a few picoseconds; and (*iii*) slower oscillation coupled with relaxation on the time scale of several picoseconds. These three features of the ultrafast decay of Au/glass are consistent with visible pump/white light probe data previously reported for Au nanopyramids supported on glass by nanosphere lithography, and the overall data is consistent with ultrafast decay of Au nanoparticles.[21] Accordingly, we attribute the ultrafast response of our Au/glass sample based on previous work. Specifically, the initial sub-50 fs decay is associated with dephasing of coherently excited non-thermal distribution of conduction electrons followed by thermalization via electron-electron scattering with a 170 fs time constant. The subsequent decay with time constant of 5.6 ps is associated with electron-phonon coupling leading to heating of the lattice.

A two-temperature model is employed to describe the thermal evolution of electron and lattice (phonon) temperatures. In this model, pump pulse energies are absorbed by the nanoparticles, thus creating a population of hot conduction electrons. Electron-phonon coupling mediates energy exchange between conduction electrons and the nanoparticle lattice. Thermal equilibrium is reached by phonon-phonon scattering which allows heat exchange between the nanoparticle and the surrounding environment. Thus, the electron and lattice temperatures

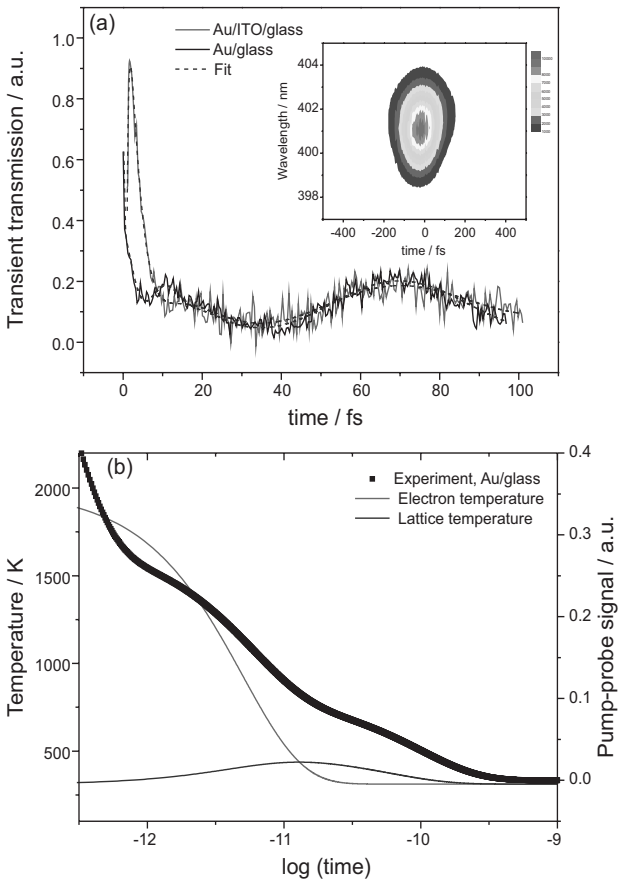


**Figure 4.** (a) Pump-probe signal *vs.* time delay for Au/glass (black curve) and Au/ITO/glass (red curve). Pump energy: 10 nJ; probe energy: 2 nJ. Pump and probe wavelengths are centered around 800 nm. Inset: frequency-resolved optical gating trace showing 50 fs time resolution. (b) Thermal evolution of electron (red curve) and lattice (blue curve) temperatures obtained by numerical solution of the two-temperature model. Black squares: exponential decay component of the Au/glass pump-probe signal shown in (a).

**Table 1.** Least-squares nonlinear curve fit to the pump-probe data presented in Figures 4a and 5b

| Sample | Au/glass | | | Au/ITO/glass | | |
|---|---|---|---|---|---|---|
| Wavelength / nm | 750 | 800 | 870 | 800 | 870 | 915 |
| Pulse duration / ps | 0.11 | 0.052 | 0.084 | 0.052 | 0.084 | 0.06 |
| $a_1$ | 0.02 | 0.005 | 0.016 | 0.003 | 0.525 | 0.206 |
| $\tau_1$ / ps | < 0.1 | < 0.05 | < 0.08 | < 0.05 | < 0.08 | < 0.06 |
| $a_2$ | –0.08 | 0.820 | 0.26 | –9.75 | 0.03 | 1.68 |
| $\tau_2$ / ps | 0.190 | 0.170 | 0.25 | 0.42 | 0.30 | 0.27 |
| $a_3$ | 0.32 | 0.190 | –0.16 | 1.43 | 0.02 | –0.34 |
| $\tau_3$ / ps | 2.96 | 5.600 | 2.70 | 3.73 | 2.38 | 3.08 |
| $a_4$ | – | 0.090 | – | 0.09 | – | – |
| $\tau_4$ / ps | – | 284 | – | 138 | – | – |
| $T_1$ / ps | – | 12.36 | – | 30.96 | – | – |
| $T_2$ / ps | – | ca. 70 | – | ca. 70 | – | – |
| $R^2$ | 0.990 | 0.892 | 0.895 | 0.994 | 0.949 | 0.931 |

ITO: indium tin oxide; $a_1$-$a_4$: amplitude; $\tau_1$-$\tau_4$: time-constant; $T_1$ and $T_2$: oscillation period; $R^2$: coefficient of determination.

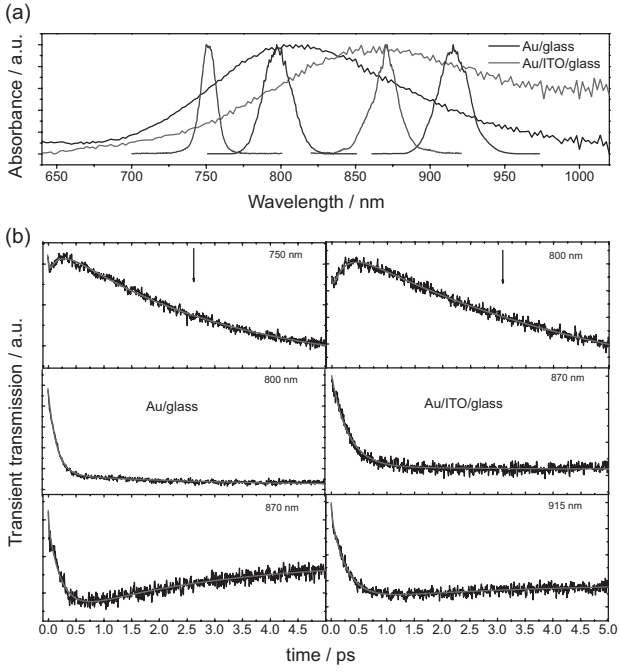


**Figure 5.** Wavelength-dependent one-color pump-probe signal for Au/glass and Au/ITO/glass. (a) Linear absorption spectra of Au/glass (black curve) and Au/ITO/glass (red curve) overlapped with laser spectra centered at 915 nm (violet), 870 nm (green), 800 nm (blue) and 750 nm (cyan). (b) Panel showing the pump-probe signals for Au/glass (left column) and Au/ITO/glass (right column). On the left column, the three figures respectively show the pump-probe signals measured at 750, 800, and 870 nm. On the right column, the three figures respectively show the pump-probe signals measured at 800, 870, and 915 nm. Pump energy: 10 nJ; probe energy: 2 nJ. Pump and probe wavelengths are centered around 800 nm. See Table 1 for time resolution data.

($T_e$ and $T_l$, respectively) are described by a coupled pair of differential equations:

$$C_e(T_e)\frac{\partial T_e}{\partial t} = -G_{e-ph}\left(T_e - T_l\right) \quad (1)$$

$$C_l\frac{\partial T_l}{\partial t} \approx G_{e-ph}\left(T_e - T_l\right) - G_{ph-ph}\left(T_l - T_0\right) \quad (2)$$

The electron heat capacity ($C_e$) is assumed proportional to temperature with proportionality equal to 71.5 J $m^{-3}$ $K^{-2}$. The heat capacity is assumed to be a constant, $C_l = 3k_B n$, where $k_B$ is Boltzmann's constant and $n$ is the atomic density of gold. Electron-phonon and phonon-phonon coupling coefficients ($G_{e-ph}$ and $G_{ph-ph}$, respectively) were chosen to reproduce our measured electron-phonon and phonon-phonon relaxation times. These differential equations were solved numerically employing the following initial conditions: $T_l = T_0 = 300$ K, $T_e = 2000$ K (10 nJ *per* pulse).

As shown in Figure 4b, electrons and phonons reach thermal equilibrium on the time scale of a few picoseconds, returning to room temperature on the time scale of hundreds of picoseconds. The exponential decay part of the 800 nm pump-probe signal for Au/glass is overlaid in Figure 4b to aid visual comparison with the two-temperature model numerical results. Good agreement between experimental data and numerical results indicate that the thermal evolution of electron and phonon baths can be adequately used to describe our measured pump-probe signals. The major qualitative differences between model and experiment occur at both very short and very long timescales. On the femtosecond timescale electron dynamics is governed by coherent oscillation of conduction electrons. The slower response of several picoseconds is associated with lattice cooling together with mechanical expansion and contraction of the entire lattice, leading to acoustic oscillations on the time scale of several picoseconds. The short-time electron dynamics and the long-time damped acoustic oscillations are not captured by our purely kinetic two-temperature model.

The pump-probe signal oscillations for Au/glass shown in Figure 4a are consistent with overall good uniformity in particle sizes and shapes at the length scale of several microns. That is, acoustic oscillations of nanoparticles of differing sizes would be out-of-phase with each other thereby very quickly damping any oscillations in the pump-probe signal. Thus, we conclude that our pump-probe results and interpretation are consistent with previous ultrafast dynamics work on gold triangular nanoprism arrays prepared by nanosphere lithography.[21-23] We also conclude that the sample imperfections shown in the AFM images (Figure 2) did not affect the reproducibility of the ultrafast data reported herein.

Pump-probe data for Au/ITO/glass at 800 nm center wavelength is also shown in Figure 4a (red curve). As in the Au/glass system, we observe (*i*) a nearly instantaneous rise/decay following the instrument response function; (*ii*) subsequent relaxation on the femtosecond/picosecond timescales; and (*iii*) slower oscillation coupled with relaxation on the time scale of several picoseconds. However, unlike in the Au/glass system, in the case of Au/ITO/glass we observe a rise in the transient transmission signal following the instantaneous rise and decay at time-zero. The signal rise and slow decay observed for Au/ITO/glass and the contrast with the Au/glass pump-probe data are more clearly seen in Figure 5b, which displays experimental results for the first 3 ps following pump pulse excitation. The maximum in the transient transmission signal is observed ca. 500 fs after time zero with a ca. 400 fs time constant associated with signal rise. Afterwards, the pump-probe signal decays with a 3.7 ps time constant. At longer timescales, the pump-probe signal amplitude and oscillation follow the same dynamics as observed for the

Au/glass sample. Thus, by looking only at the 800 nm pump-probe data shown in Figure 4a, it seems at first glance that ultrafast dynamics in Au/ITO/glass and Au/glass are qualitatively different. However, subsequent wavelength-dependent pump-probe measurements and four-wave mixing measurements show that the short-time dynamics are qualitatively similar for both systems, as shown below.

In order to gain further insight into the ultrafast dynamics in Au/glass and Au/ITO/glass systems, we have performed one-color pump-probe measurements at a range of wavelengths spanning the linear absorption spectra of each of these two systems. Wavelength tuning of the femtosecond laser source was achieved by employing an optical parametric amplifier as described in Experimental. Figure 5a shows an overlap of the linear absorption spectra of Au/glass and Au/ITO/glass with the laser spectra employed in the pump-probe measurements. For each sample, we have conducted one-color pump-probe measurements at three different wavelengths: (*i*) 750, 800, and 870 nm for Au/glass which has a resonance at 800 nm; (*ii*) 800, 870, and 915 nm for Au/ITO/glass which has a resonance at 870 nm. The complex frequency-dependent material response of a system can be described as the sum of refractive index (real part) and absorption (imaginary part). Given the large light scattering in plasmonic nanoparticles, it is important to assess the relative importance of dispersive and absorptive contributions to our measured signals, both on- and off-resonance. Starting from either absorption or refractive index data alone, determination of the full complex response function can be obtained indirectly via Kramers Kronig transformation. Alternatively, the full complex response may be retrieved experimentally, for example, by employing four-wave mixing spectroscopy with optical heterodyning or spectral interferometry detection.

Figure 5b shows wavelength-dependent pump-probe transients for Au/glass (left column) and Au/ITO/glass (right column). Table 1 summarizes the parameters obtained by nonlinear least-squares data fitting. In the case of Au/glass below the surface plasmon resonance center wavelength, the pump-probe transient transmission signal at 750 nm exhibits an ultrafast response with 190 fs time constant associated with electron-electron scattering, followed by 2.96 ps electron-phonon time decay. The pump-probe data measured employing a center wavelength of 800 nm, which is the surface plasmon resonance wavelength for Au/glass, exhibits the same dynamics shown in Figure 4. Finally, above the surface plasmon resonance, the pump-probe signal at 870 nm for Au/glass exhibits a 250 fs decay time for electron-electron scattering followed by electron-phonon coupling with 2.7 ps time constant.

In the case of Au/ITO/glass below the surface plasmon resonance, the pump-probe signal at 800 nm shown in Figure 5b corresponds to the first 3 ps of the pump-probe signal shown in Figure 4a. The data is reproduced in Figure 5b to aid visual comparison with pump-probe signals measured at different wavelengths. At 870 nm, the surface plasmon resonance wavelength for Au/ITO/glass, the pump-probe signal decays due to electron-electron scattering with 300 fs time constant, followed by electron-phonon coupling time constant of 2.4 ps. Finally, above the surface plasmon resonance, the pump-probe signal at 915 nm for Au/ITO/glass exhibits a 270 fs time constant associated with electron-electron scattering and the subsequent electron-phonon coupling decay is observed with a ca. 3 ps time constant.

Overall, a qualitative analysis of the one-color pump-probe signals shown in Figure 5b for Au/glass and Au/ITO/glass indicates that these two systems exhibit similar wavelength-dependent ultrafast dynamics. For instance, the pump-probe experiments performed below the surface plasmon resonance (panel in Figure 5b, first row) exhibited an ultrafast rise in the signal followed by slower decay on the time scale of a few picoseconds; qualitatively, the same transient response was observed for both Au/glass and Au/ITO/glass. By the same token, when performing experiments at the surface plasmon resonance wavelength of each of these two systems (panel in Figure 5b, second row), the pump-probe signal decays on a sub-picosecond timescale followed by a small amplitude decay of a few picoseconds. Finally, in the experiments performed above the surface plasmon resonance wavelength for both Au/glass and Au/ITO/glass, we measured a sub-picosecond decay followed by a picosecond decay with a small negative amplitude.

The experimental and simulated linear optical spectra shown in Figure 3 indicated a plasmon frequency redshift in going from Au/glass to Au/ITO/glass, which was attributed primarily to differences in refractive index of glass *vs.* ITO. Similarly, the pump-probe results shown in Figure 5b may also be explained by assuming a redshift of the plasmon resonance for Au/glass *vs.* Au/ITO/glass due to the higher refractive index of ITO. Pump-probe experiments are unable to separate the real and imaginary parts of the third-order polarization that gives rise to the observed signals shown in Figures 4a and 5b. At resonance, the absorptive part may be the dominant contribution to the pump-probe signal, whereas away from resonance the dispersive part presumably also contributes to the observed signal. A phase shift of ca. $\pi$ in the pump-probe signal is observed in our results shown in Figure 5b: an ultrafast transient rise is observed below resonance whereas an

ultrafast decay with a change in sign of the pump-probe signal is observed above resonance. Assuming a dipolar picture of matter-radiation interaction, a forced harmonic oscillator with damping exhibits a frequency dependent phase shift described by

$$\tan\varphi = \frac{2\gamma\omega}{\omega_o^2 - \omega^2} \quad (3)$$

where $\phi$ is the harmonic oscillator phase, $\gamma$ is the damping factor, $\omega$ is the angular frequency and $\omega_0$ is the natural frequency. Hence, a phase shift of $\pi$ is expected as the oscillator is driven at different frequencies that span its natural frequency. Depending on the damping, such a phase shift may be observed near resonance. For example, assuming a linewidth of 100 nm for the linear spectra shown in Figures 3 and 5a, we estimate a phase shift of 0.75$\pi$ between 870 and 750 nm for Au/glass with a resonance at 800 nm, and a phase shift of 0.73$\pi$ between 915 and 800 nm for Au/ITO/glass with a surface plasmon resonance at 870 nm. These estimates provide a lower bound to the actual phase shift since the homogeneous linewidth will likely be narrower than the linewidths shown in Figures 3 and 5b. Incidentally, this effect has been explored in the study of surface-plasmon absorption-induced optical forces, where attractive and repulsive plasmonic interactions can be observed depending on whether the incident light is on the red- or blue-side of the surface plasmon resonance, respectively.[15]

The one-color pump-probe measurements performed across the surface plasmon resonance thus reflect the material wavelength-dependent complex refractive index. In order to further test whether the same mechanism underlies the ultrafast dynamic response in both systems, we have performed time-resolved four-wave mixing spectroscopy at 800 nm center wavelength on Au/glass and Au/ITO/glass. Figure 6a schematically shows the four-wave mixing apparatus, and Figure 6b shows the absorptive and dispersive parts of the four-wave mixing signal for each of these two samples.

As shown in Figure 6, the absorptive four-wave mixing signal is positive for both samples. On the other hand, the dispersive four-wave mixing signal is negative (except near time-zero) for Au/glass and nearly zero for Au/ITO/glass. The on-resonance dispersive signal for Au/glass at 800 nm (Figure 6b, blue curve) is similar to the Au/glass pump-probe signal at 870 nm (Figure 5b), and the on-resonance absorptive signal of Au/glass at 800 nm (Figure 6b, black curve) resembles the resonant pump-probe signal at 800 nm. Similarly, for Au/ITO/glass, our four-wave mixing experiments performed at 800 nm can be compared with the wavelength-dependent pump-probe

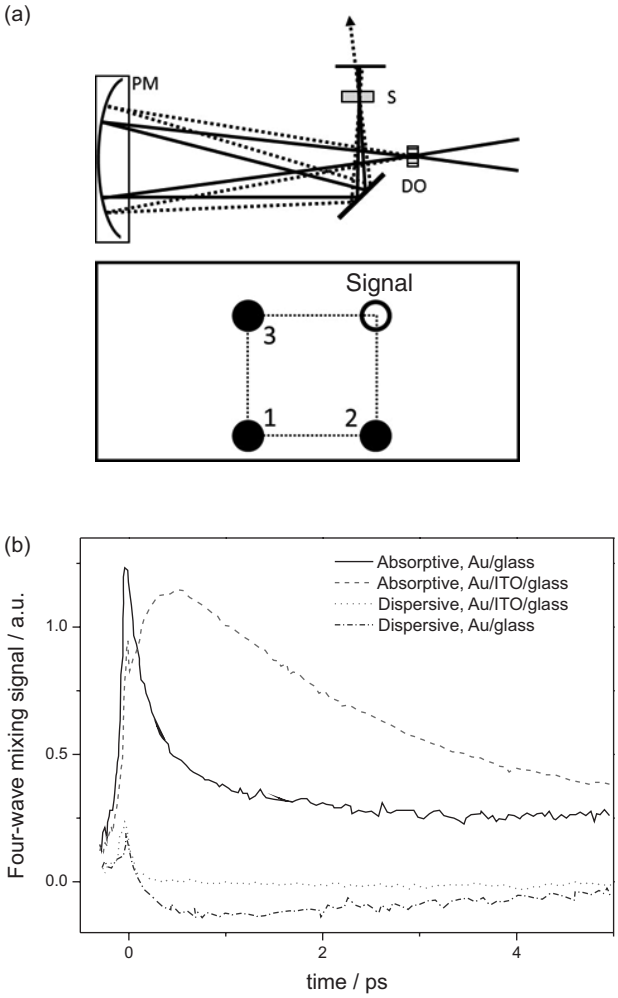


**Figure 6.** (a) Diffractive-optic four-wave mixing spectroscopy. Top: apparatus layout. DO: diffractive optic; PM: parabolic mirror; S: sample. Bottom: front view after the sample, indicating pulses 1, 2, 3, and the signal. (b) Four-wave mixing signals at 800 nm center wavelength for Au/glass (absorptive: black curve; dispersive: blue curve) and Au/ITO/glass (absorptive: red curve; dispersive: magenta curve).

signals shown in Figure 5b. That is, for Au/ITO/glass, the off-resonance dispersive four-wave mixing signal at 800 nm (Figure 6b, magenta curve) is similar to the pump-probe signal at 870 nm (Figure 5b) due to the light-absorption-induced redshift of the surface plasmon resonance. In turn, the off-resonance absorptive four-wave mixing signal at 800 nm (Figure 6b, red curve) is similar to the transient-transmission pump-probe signal at 800 nm. Upon light absorption by the nanoparticles, thermal evolution of electron and lattice temperatures alter the complex material dielectric function thereby leading to frequency shifts and spectral broadening of the surface plasmon resonance. The four-wave mixing signals can thus be interpreted assuming that surface plasmon absorption changes as a function of electron temperatures, when compared to room temperature. Specifically, light absorption leads to surface plasmon resonance redshift, which is manifested

as a change in the transient dispersive contribution to the four-wave mixing signal. Light absorption also leads to spectral broadening, which in turn leads to changes in the absorptive part of the four-wave mixing signal.[24]

Overall, the results shown in this work indicate that one-color pump-probe and four-wave mixing signals are dominated by the frequency- and temperature-dependent complex material dielectric function. We have been unable to observe an additional contribution to the observed signals that could be attributed to charge transfer/injection into ITO. Recently, charge injection from metal nanoparticles into ITO have been observed with picosecond time-resolved microscopy.[11] Specifically, Muskens and co-workers[11] have employed two-color picosecond pump-probe measurements on single metal nanoparticles whereby a visible pump laser excites the metallic nanoparticles at the plasmon resonance frequency whereas a near-infrared pulse probed free carrier absorption around the ITO bandgap. Fast hot-electron injection from the gold antenna was observed, followed by thermalization and a local reduction of the ITO free-carrier density. Thus, in order to observe ultrafast plasmon frequency shifts due to charge transfer in the nano-structures discussed in our work presented here, one may need to perform two-color transient absorption measurements probing at longer wavelengths and employing smaller metallic nanoparticles to minimize the strong scattering signal associated with hot electrons.

## Conclusions

We have described the preparation and characterization of arrays of isolated Au triangular nanoprisms over glass and a thin layer of ITO by nanosphere lithography. The linear absorption spectra of Au/glass and Au/ITO/glass exhibit surface plasmon resonances at 800 and 870 nm, with a 70 nm redshift associated with the refractive index of ITO. We have performed one-color pump-probe and four-wave mixing measurements with femtosecond time resolution at wavelengths below the surface plasmon resonance, at resonance, and above the surface plasmon resonance for each of these two systems. The ultrafast dynamics on both systems can be described by a model accounting for electron-electron scattering, electron-phonon coupling, and acoustic oscillations on top of cooling of the gold lattice. The wavelength-dependent results are described in terms of the complex wavelength-dependent refractive index of gold, which modulates the measured pump-probe signals. This interpretation is consistent with comparative measurements of absorptive and dispersive parts of the four-wave mixing signals at 800 nm.

## Experimental

### Sample preparation

Monodisperse PS microspheres with 476 ± 14 nm diameter were purchased from Microparticles GmbH as 10 wt.% in aqueous solution. Optically transparent ITO films (Delta Technologies Ltd.) with coating thickness 190 nm and sheet resistance of 4-8 Ω cm were used as substrate. Bidistilled and de-ionized water was used in all fabrication stages. Colloidal masks with one monolayer were crystallized on top of ITO substrates by spin coating at 1400 rpm during 2 min. Prior to mask fabrication, ITO substrates were rendered hydrophilic by chemical oxidation: 1 h in $NH_4OH$, $H_2O_2$ and $H_2O$ (1:1:5 ratio) at 82 °C. After spin coating, the masks were dried in air for 24 h at 60 °C to improve adhesion.

The nanostructures constructed by using colloidal masks depend mainly on the kind of infiltration mechanism used (e.g., evaporation, sol-gel, electroplating, etc.). In our case, 50 nm of Au were evaporated on the mask. The colloidal mask was removed by immersion in toluene for 30 min. We obtained an ordered array of Au islands with triangular forms on the ITO substrates (see Results and Discussion). Linear absorption measurements were performed in a standard transmission mode using UV-Vis Hitachi U-2900 spectrophotometer.

### Discrete dipole approximation simulations

The extinction spectra were simulated by the DDA method. Briefly, the method describes the target nanostructure by an array of N polarizable dipoles, whose induced dipole moment ($\vec{P}_j$) can be written as:[25]

$$\vec{P}_j = \alpha_j \times \vec{E}_{loc}(r_j) \quad (4)$$

where $\vec{E}_{loc}(r_j)$ is the local electric field at the position of the j$^{th}$ dipole and $\alpha_j$ is the polarizability at that point. This local field corresponds to the sum of incident ($\vec{E}_0$) and scattered electric fields by each of the dipoles in the target. Therefore, the fundamental quantity to be described is the material polarizability, which can be described in a first approximation in terms of the material dielectric function by means of the Clausius-Mossotti relation:[1]

$$\alpha_j^{CM} = \frac{3d^3}{4\pi}\frac{\varepsilon_j - 1}{\varepsilon_j + 2} \quad (5)$$

where $\alpha_j^{CM}$ is the Clausius-Mossotti polarizability at the j$^{th}$ dipole, d is the diameter of the dipole and $\varepsilon_j$ is the dielectric permittivity of the j$^{th}$ dipole.

For all DDA simulations in this work, the dielectric function values were taken from experimental results. In the case of Au, it was considered the compilation from Johnson and Christy.[26] We also used experimental data provided by König *et al.*[27] and Rubin[28] for ITO and glass, respectively, which are presented in the inset of Figure 3b.

After reaching convergence for the induced dipoles, the extinction coefficient ($s_{ext}$) for each incident light wavelength (and therefore each wave-vector, **k**) is given by:

$$\sigma_{ext} = \frac{4\pi k}{\left|\vec{E}_0\right|^2} \sum_{j=1}^{N} \mathrm{Im}(\vec{E}^*_{0,j} \times \vec{P}_j) \quad (6)$$

AFM measurements indicate that tip-to-tip distance between neighboring nanoparticles is greater than 50 nm on average, and thus coupling effects among Au nanostructures in the prepared sample can be neglected (see below). Therefore, simulations were performed for a single Au island on top of a cylindrical slab with diameter of 320 nm and height of 60 nm, following the protocol described by Schatz and co-workers.[29] The geometry employed in our DDA simulations is depicted in Figure 2c.

### Pump-probe spectroscopy

The pump-probe experiments were carried out using femtosecond pulses generated in a commercial Ti:sapphire laser (Legend, Coherent) operating at 1 kHz repetition rate. The amplifier output is used to pump an optical parametric amplifier (OPERA, Coherent) generating 50 fs pulses tunable from the visible to the near-IR. The pulse duration was characterized at the sample position employing a home-built frequency-resolved optical gating apparatus, as shown in the inset of Figure 4a. In our one-color pump-probe experiments, we have employed four distinct center wavelengths of the femtosecond pulses: 750, 800, 870, and 915 nm. The linear vertical polarization of pump and probe beams was independently set by half-wave plate and polarizer combination. Changing the light polarization of the pump and probe pulses did not provide additional insights, presumably due to the absence of interparticle coupling effects and the overall isotropic structure of the nanoparticle array. Typically, 10 nJ are split into pump (90%) and probe (10%) beams. A 40 cm focal-length lens was used to focus both pump and probe beams on the sample. The sample was placed on a manual xyz-linear translation stage, which was kept fixed in position during the ultrafast experiments. To enhance the signal detection sensitivity, we have used lock-in amplification with an optical chopper operating at 90 Hz.

We comment on our efforts aimed at avoiding laser-induced destruction of the nanostructures. First, given the pump pulse energy, pulse duration, and beam size at the focus, the peak intensities of pump pulses employed in our work are approximately 2 GW cm$^{-2}$. By contrast, literature reports of laser-induced degradation and/or reshaping of metallic nanoparticle arrays prepared by nanosphere lithography employed peak intensities higher than that used in the present work.[30,31] Second, in order to verify the maximum pump pulse energy that could be employed without leading to laser-induced sample degradation, we performed repeated pump-probe scans at a range of pump pulse energies. At pump energies near 10 nJ *per* pulse, pump-probe scans could be measured repeatedly, thereby indicating absence of sample degradation.[30] On the other hand, above 90 nJ *per* pulse pump energies, pump-probe scans could not be reproduced reliably. In the Results and Discussion, pump-probe transients are reported for 10 nJ *per* pulse pump energy, which is nine times lower than our damage threshold. Third, we performed optical spectroscopy and electron microscopy measurements on the samples before and after the pump-probe measurements. The beams employed in the pump-probe experiments reported here had an area of approximately 40 μm × 40 μm at the focus, thus optical spectroscopy and electron microscopy experiments sampled multiple particles at a time.[30]

### Four-wave mixing spectroscopy

The four-wave mixing apparatus was built to allow separate mesaurements of the real (dispersive) and imaginary (absorptive) parts of complex wavelength-dependent material response. Briefly, two laser pulses are incident on a diffractive optic (Holoeye Photonics) designed to produce pulse pairs 1 and 2 (pump 1 and pump 2), and 3 and 4 (probe and local oscillator, respectively). The resulting boxcar pattern is imaged onto the sample with a combination of on-axis parabolic mirrors (Edmund, 17 inch focal lengths). The four-wave mixing apparatus is designed in a transient grating configuration whereby pulses 1 and 2 arrive at the sample at the same time, and the time delay between pulses 1 and 2 and pulse 3 is controlled before the diffractive optic. The probe beam is scattered off the holographic grating induced in the sample, and the resulting four-wave mixing signal is detected in the phase-matched direction, collinear with the local oscillator (see Figure 6a). Optical heterodyne detection is employed. The same pulse energies employed in the pump-probe experiments are employed in the four-wave mixing experiments.

## Acknowledgements

We gratefully acknowledge financial support from FAPESP (grants 2008/10593-0, 2015/08831-4). We have built the time-resolved ultrafast spectroscopy instruments described in this work in the femtosecond laser laboratory of Carlos H. Brito-Cruz and we gratefully acknowledge his assistance, kind support and laser time. We also gratefully acknowledge Cristiano M. B. Cordeiro and Teresa D. Z. Atvars for their support in earlier stages of this research.

## References

1. Novotny, L.; Hecht, B.; *Principles of Nano-Optics*, 2nd ed.; Cambridge University Press: Cambridge, 2012.
2. Stewart, M. E.; Anderton, C. R.; Thompson, L. B.; Maria, J.; Gray, S. K.; Rogers, J. A.; Nuzzo, R. G.; *Chem. Rev.* **2008**, *108*, 494.
3. Bardhan, R.; Lal, S.; Joshi, A.; Halas, N. J.; *Acc. Chem. Res.* **2011**, *44*, 936.
4. Jain, P. K.; Huang, X. H.; El-Sayed, I. H.; El-Sayed, M. A.; *Acc. Chem. Res.* **2008**, *41*, 1578.
5. Petri, M. V.; Ando, R. A.; Camargo, P. H. C.; *Chem. Phys. Lett.* **2012**, *531*, 188.
6. Koller, D. M.; Hohenau, A.; Ditlbacher, H.; Galler, N.; Reil, F.; Aussenegg, F. R.; Leitner, A.; List, E. J. W.; Krenn, J. R.; *Nat. Photonics* **2008**, *2*, 684.
7. Pelton, M.; Aizpurua, J.; Bryant, G.; *Laser Photonics Rev.* **2008**, *2*, 136.
8. Atwater, H. A.; Polman, A.; *Nat. Mater.* **2010**, *9*, 205.
9. O'Carroll, D.; Hofmann, C. E.; Atwater, H. A.; *Adv. Mater*. **2010**, *22*, 1223.
10. West, P. R.; Ishii, S.; Naik, G. V.; Emani, N. K.; Shalaev, V. M.; Boltasseva, A.; *Laser Photonics Rev.* **2010**, *4*, 795.
11. Abb, M.; Albella, P.; Aizpurua, J.; Muskens, O. L.; *Nano Lett.* **2011**, *11*, 2457.
12. Du, L.; Furube, A.; Hara, K.; Katoh, R.; Tachiya, M.; *J. Photochem. Photobiol., C* **2013**, *15*, 21.
13. Bairu, S. G.; Mghanga, E.; Hasan, J.; Kola, S.; Rao, V. J.; Bhanuprakash, K.; Giribabu, L.; Wiederrecht, G. P.; da Silva, R.; Rego, L. G. C.; Ramakrishna, G.; *J. Phys. Chem. C* **2013**, *117*, 4824.
14. Huang, W.; Qian, W.; El-Sayed, M. A.; Ding, Y.; Wang, Z. L.; *J. Phys. Chem. C* **2007**, *111*, 10751.
15. Nome, R. A.; Guffey, M. J.; Scherer, N. F.; Gray, S. K.; *J. Phys. Chem. A* **2009**, *113*, 4408.
16. Huang, W.; Qian, W.; El-Sayed, M. A.; *J. Phys. Chem. B* **2005**, *109*, 18881.
17. Mulvaney, P.; *Langmuir* **1996**, *12*, 788.
18. Kelly, K. L.; Coronado, E.; Zhao, L. L.; Schatz, G. C.; *J. Phys. Chem. B* **2003**, *107*, 668.
19. Lu, X. M.; Rycenga, M.; Skrabalak, S. E.; Wiley, B.; Xia, Y. N.; *Annu. Rev. Phys. Chem.* **2009**, *60*, 167.
20. Mahmoud, M. A.; Chamanzar, M.; Adibi, A.; El-Sayed, M. A.; *J. Am. Chem. Soc.* **2012**, *134*, 6434.
21. Huang, W.; Qian, W.; El-Sayed, M. A.; *Nano Lett.* **2004**, *4*, 1741.
22. Sonnichsen, C.; Franzl, T.; von Plessen, G.; Feldmann, J.; Wilson, O.; Mulvaney, P.; *Phys. Rev. Lett.* **2002**, *88*, 077402.
23. Hu, M.; Novo, C.; Funston, A.; Wang, H. N.; Staleva, H.; Zou, S. L.; Mulvaney, P.; Xia, Y. N.; Hartland, G. V.; *J. Mater. Chem.* **2008**, *18*, 1949.
24. Park, S.; Pelton, M.; Liu, M.; Guyot-Sionnest, P.; Scherer, N. F.; *J. Phys. Chem. C* **2007**, *111*, 116.
25. Draine, B. T.; Flatau, P. J.; *J. Opt. Soc. Am. A* **1994**, *11*, 1491.
26. Johnson, P. B.; Christy, R. W.; *Phys. Rev. B: Solid State* **1971**, *6*, 4370.
27. König, T. A. F.; Ledin, P. A; Kerszulis, J.; Mahmoud, M. A.; El-Sayed, M. A.; Reynolds, J. R.; Tsukruk, V. V.; *ACS Nano* **2014**, *8*, 6182.
28. Rubin, M.; *Sol. Energy Mater.* **1985**, *12*, 275.
29. Duval Malinsky, M.; Kelly, K. L.; Schatz, G. C.; Van Duyne, R. P.; *J. Phys. Chem. B* **2001**, *105*, 2343.
30. Tabor, C.; Qian, W.; El-Sayed, M. A.; *J. Phys. Chem. C* **2007**, *111*, 8934.
31. Huang, W.; Qian, W.; El-Sayed, M. A.; *J. Appl. Phys.* **2005**, *98*, 114301.

*Submitted: August 21, 2015*
*Published online: December 4, 2015*

**FAPESP has sponsored the publication of this article.**